

Article

Correlating Disorder Microstructure and Magnetotransport of Carbon Nanowalls

Mijaela Acosta Gentoiu ¹, Rafael García Gutiérrez ² , José Joaquín Alvarado Pulido ¹, Javier Montaña Peraza ², Marius Volmer ³ , Sorin Vizireanu ⁴ , Stefan Antohe ⁵ , Gheorghe Dinescu ⁴  and Ricardo Alberto Rodríguez-Carvajal ^{6,*} 

¹ Science Institute, Meritorious Autonomous University of Puebla, Puebla 72570, Mexico

² Departamento de Investigación en Física, Universidad de Sonora, Hermosillo 83000, Mexico

³ Department of Electrical Engineering and Applied Physics, Transilvania University of Brasov, Blvd. Eroilor 29, 500036 Brasov, Romania

⁴ National Institute for Lasers, Plasma and Radiation Physics, 409 Atomistilor Street, Magurele, 077125 Bucharest, Romania

⁵ Faculty of Physics, University of Bucharest, 405 Atomistilor Street, 077125 Bucharest, Romania

⁶ Campus Guanajuato, Universidad de Guanajuato, Noria Alta S/N, Guanajuato 36250, Mexico

* Correspondence: rodriguez.ricardo@ugto.mx

Abstract: The carbon nanowalls (CNWs) grown by Plasma-Enhanced CVD reveal differences in the magnetotransport properties depending on the synthesis parameters. In this paper, we report the influence of the deposition temperature, which produces variations of the disorder microstructure of the CNWs. Relative low disorder leads to the weak localization with the transition to weak antilocalization. Higher disorder generates positive Hopping mechanism in low field with a crossover to a diffusion transport by graphene nanocrystallites. The samples reveal a similitude of the isoline density of the MR at a low temperature (<50 K), explained in the context of the magnetization. This effect is independent of the number of defects. We can achieve a desirable amount of control over the MT properties changing the CNWs' microstructure.

Keywords: magnetotransport; graphene; nanowalls; disorder



Citation: Acosta Gentoiu, M.; García Gutiérrez, R.; Alvarado Pulido, J.J.; Montaña Peraza, J.; Volmer, M.; Vizireanu, S.; Antohe, S.; Dinescu, G.; Rodríguez-Carvajal, R.A. Correlating Disorder Microstructure and Magnetotransport of Carbon Nanowalls. *Appl. Sci.* **2023**, *13*, 2476. <https://doi.org/10.3390/app13042476>

Academic Editors: Francesco Tornabene and Rossana Dimitri

Received: 25 December 2022

Revised: 3 February 2023

Accepted: 6 February 2023

Published: 14 February 2023



Copyright: © 2023 by the authors. Licensee MDPI, Basel, Switzerland. This article is an open access article distributed under the terms and conditions of the Creative Commons Attribution (CC BY) license (<https://creativecommons.org/licenses/by/4.0/>).

1. Introduction

The special magnetotransport (MT) properties of graphene-based nanostructures have received considerable attention in the last years. The uncommon Dirac point [1], chiral nature [2] and Berry's phase [3] lead to different MT properties compared to the conventional two-dimensional (2D) systems. The graphene presents an unconventional weak antilocalization (WAL) due to the Berry's phase π in a valley, which adds a quantum phase when two electron waves circulate in a reverse closed path, producing a suppression of backscattering [4]. The magnetotransport properties in graphene materials can be modified by the arrangement of sheets, particle size [5], disorder such as curvature, topological defects [6], geometry of the graphene edges, localized magnetic moment [7] and boundaries and interfaces [8].

Large 3D graphene networks, in contrast to 1D and 2D graphene-based nanostructures, easily allow us to modify the trajectories of carriers in a magnetic field to obtain a specific desirable MT behavior. There are not many studies related to the MT properties of 3D carbon nanowalls (CNWs), although these structures have other remarkable applications, such as catalyst supports, high sensitivity gas detection [9], biosensors [10] and supercapacitors [11,12]. Thus, completing the range of applications with those related to MT is a new direction for the exploration of the applicative potential of CNW materials. In MT research, we can mention Yue et al. [13], who obtained control over the magnetoresistance (MR) changing the morphology of the CNWs; and Huang et al. [14] in aligned walls.

The CNWs consist of stacks of a few vertical graphene layers in a self-supported network [15]. As a consequence, the sheets behave like freestanding ones [16], with a weak influence of the substrate. This advantage allows rigorously identify the intrinsic MT mechanism at difference of the graphene attached over a supporting substrate. Specifically, the quantum interference correction to the magnetotransport and the influences of the nature of disorder are currently lacking.

The deposition of CNWs is not straightforward and only a few methods are available. Zhang's group [17] obtained the CNWs via RF sputtering, with the disadvantage of a long deposition time (3 h). Shang's group [18], using the hot filament chemical vapor deposition (HFCVD) technique, needed catalysts or surface pretreatment. However, the Plasma-Enhanced Chemical Vapor Deposition (PECVD) is a typical and promising technique that does not require a catalyst [19] to grow with huge surface-to-mass ratio the CNWs [20] in a relatively low temperature (600–700 °C) and short time (~1 h). Davami et al. [21] stated that the deposition temperature is small compared to other synthesis methods, and numerous substrates (Ni, Ti, Pt, Cu, Ge, W, Ta, SiO₂, Al₂O₃, Cu, Si, SiO₂, stainless steel, carbon paper and others) can be used. Vizireanu et al. [22] showed that the morphology of CNWs does not change significantly when they are synthesized on substrates with different characteristics. In addition, the surface morphology and internal structure of the sample are effectively controlled.

The PECVD technique can generate CNWs with different morphologies (including petal-like, cauliflower-like and maze-like) depending on the deposition parameters, such as: temperatures and gaseous plasma (containing hydrogenated carbon precursors) [23]. The growth rate of CNWs (around tens of nanometers per minute) creates a difficulty for practical applications; however, Zhang et al. [23] improved it by increasing the RF power and CH₄ flow rate. In this sense, the morphology and microstructure of the CNWs can be easily tunable through the PECVD method. In addition, CNWs could offer a new perspective for the reproducibility of MR devices, in contrast to the few-layer graphene grown by CVD, where the thickness is not controllable yet.

In this paper, it is presented a comparative study of the MT properties between two CNW samples differentiated by the disorder and grown by the PECVD technique. The selection of these two samples, named Sample I and Sample II, was made while considering the results of a structural and morphological comparative study between CNWs' growth according to different synthesis parameters (time, Argon flux and deposition temperature (T_D)). The selected samples have structural and morphological qualities such as few graphene layers in the walls, large dimensions and a reduced contamination by hydrogen or oxygen atoms.

The disorder introduces mobility fluctuations in the magnetoresistance with the magnetic field applied. We find different magnetotransport effects as the disorder increases: weak localization and antilocalization caused by inherent defects or impurities (Sample I) and diffuse scattering from extrinsic electron scattering sites with Hopping magnetoresistance (Sample II). At a low temperature, the samples present a similar MR isoline density. The overall results could play significant roles in our understanding of the MT in graphene materials, as well as how to control the MT properties through tunable microstructure of the CNWs via the PECVD method. It leads new perspectives for magneto-electronic devices, including biosensors and magnetic field sensor [24], magnetoresistive random-access memories (MRAM), hard drives [25] and magneto-resistors for measuring electric current.

2. Experimental Section

Previous studies [26–28] have found the key to control different characteristics on the carbon nanowalls (such as length, shape and composition) through the synthesis parameters by the PECVD. We apply the following constant parameters: pressure of 120 Pa and RF power of 300 W, hydrogen/acetylene H₂:C₂H₂ = 25:1 sccm and Si/SiO₂ substrate placed at 5 cm from expansion nozzle. Table 1 shows the parameters that were varied: the ratio Argon flux at 1050 and 1400 sccm, the deposition time at 30 and 60 min, and

the deposition temperature $T_D = 600\text{ }^\circ\text{C}$ and $T_D = 700\text{ }^\circ\text{C}$. In the following, we named the samples formed at 1400 sccm-600 $^\circ\text{C}$ -1 h and 1400 sccm-700 $^\circ\text{C}$ -1 h Sample I and Sample II, respectively, due to the relevant structural and morphological characteristics to the magnetotransport studies.

Table 1. Values obtained from SEM, TEM, ERDA and Raman spectra of the CNWs formed at different synthesis parameters: time, deposition temperature and Ar flux.

Synthesis Parameters	Time (min)	30		60		
	Temperature ($^\circ\text{C}$)	700	600	Sample I 1400	1050	Sample II 1400
	Ar Flux (sccm)	1400	1050	Sample I 1400	1050	Sample II 1400
Morphology and Microstructure	Length (μm) ± 0.3	0.23	1.05	1.5	-	1.3
	Thickness (μm)	0.50	1.50	3.05	-	1.52
	$I(D)/I(G)$	2.40	1.81	1.80	2.21	2.20
	$I(D)/I(D')$	4.8	5.5	3.2	4.4	5.5
	L_a (nm)	20.4	21.0	21.1	17.2	17.3
	L_D (nm)	11.5	11.7	11.8	10.6	10.6
	2D Position (cm^{-1})	2646	2651	2646	2649	2639
	Carbon Concentration (%) by XPS	-	64.64	86.44	55.50	74.93
	Oxygen Concentration (%) by XPS	-	35.36	13.56	44.50	25.07
	Hydrogen Content by ERDA	1.4	16.7	9.1	10.1	7.8

The shape and the space between the walls of CNWs were observed by Scanning Electron Microscope (SEM), using an SEM 630 FEI Nova Nano at 10^{-4} mbar and Transmission Electron Microscope (TEM) with a JEOL 2010-F Field Emission of high resolution, operating at 200 kV. The Raman spectrum was obtained with a $\lambda_{laser} = 632.8$ nm, using a Horiba-Jobin-Yvon HR LabRAM. The Elastic Recoil Detection Analysis (ERDA) shows the hydrogen in-depth profile and concentration using 3MeV 4He^{2+} ions from a 3 MV Tandatron accelerator.

Figure 1 shows the configuration of the MR measurement, where the CNWs' samples were synthesized on four consecutive chrome-gold electrodes. The metallic strips had a gap of around 1 mm. The spacing and length of the electrodes were chosen to study the MT across a large number of CNWs junctions. The MR measurements were performed by injecting a constant electric current of 5 mA (the high value was selected due to the elevated number of walls between the electrodes). The MR behavior was not clear with values that were too small (below 1 mA). An externally relatively high magnetic field B ranging from 0 to 7 T, perpendicular to the sample's surface (parallel to the graphene layers), was applied. The temperature for measurements varied between 15 and 250 K. The MR was calculated as follows:

$$MR = \frac{R(B) - R(0)}{R(0)} \cdot 100\% \quad (1)$$

where $R(B)$ is the resistance with the magnetic field applied, while $R(0)$ is the resistance in the absence of magnetic field.

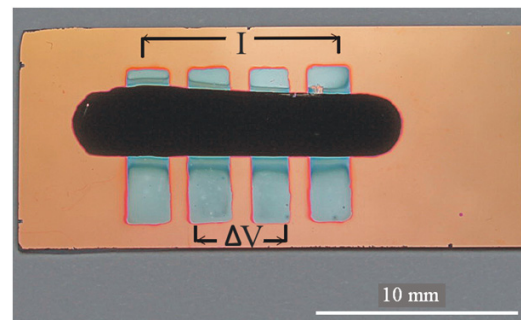


Figure 1. CNWs deposited onto electrode configurations for MR measurements.

3. Results and Discussion

3.1. Morphological and Microstructural Characteristics

Figure 2a–d present the SEM image of the CNWs formed with different parameters of synthesis: Ar flux, time and deposition temperature. In the samples synthesized at 60 min, the thickness of the walls (the longitude in the transverse direction to the substrate obtained by a cross-sectional SEM image) decrease from 3.1 to 1.5 μm , reducing the Ar flux or increasing the temperature, while the lengths of the walls became almost saturated around 1.5 μm . This suggests that, in contrast to the Ar flux, the temperature re-evaporates the nucleation sites, as is necessary for the growing of the walls. The sample formed in less time deposition, 30 min, only grows to around 0.23 μm and 0.5 μm in length and thickness, respectively. Table 1 shows a summary of the values obtained.

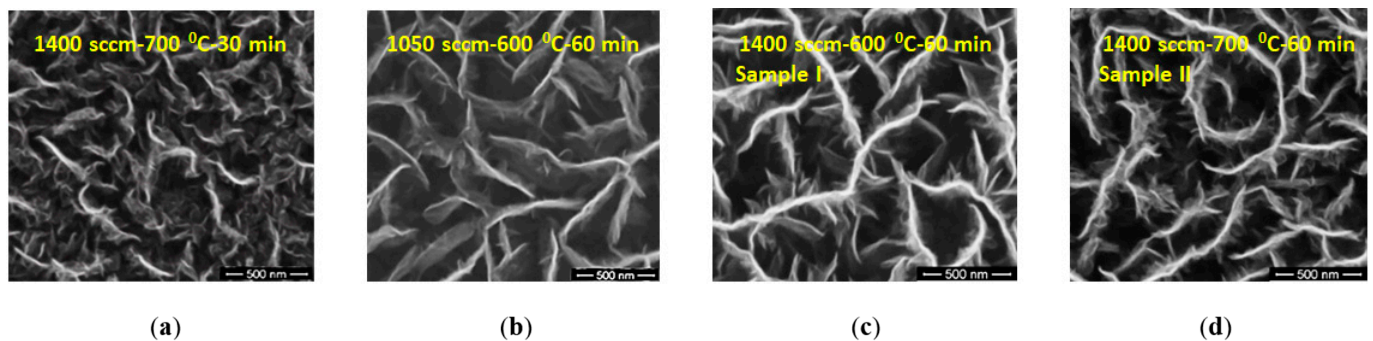


Figure 2. The SEM images for the CNWs grown at (a) 1400 sccm-700 $^{\circ}\text{C}$ -30 min, (b) 1050 sccm-600 $^{\circ}\text{C}$ -60 min, (c) 1400 sccm-600 $^{\circ}\text{C}$ -60 min and (d) 1400 sccm-700 $^{\circ}\text{C}$ -60 min.

The interlayer space of the walls varies between 0.33 and 0.35 nm, as observed in the TEM images (Figure 3a). The increase of the defect amount and temperature may break the single wall structure into many graphene nanocrystallites (GNs) (see Figure 3b,c), since each wall is composed of small graphite regions or nanographite domains [29]. The in-plane lattice constant of the GNs (observed as fringes in Figure 3c) is comparable to that of the graphite ($2.53 \pm 0.10 \text{ \AA}$ and 2.46 \AA [30], respectively). Additionally, it was found that there were nanoparticles with curved layers (see Figure 3d), similar to those obtained by Gomez-Hernandez from carbon black [31].

The Raman spectra (see Figure 4a,b) reveal a strong G-peak around 1580 cm^{-1} , which confirms the apparition of the graphene sheets and assigned to E_{2g} phonons from the Brillouin zone [32]. The D-band around 1354 cm^{-1} is activated with induced disorder. Another peak appears around 1614, named D', identified on the edges. The relation between the intensities of the peaks $I(D)/I(G)$, associated with disorder, is presented in Table 1. An increase of the values is caused by the deposition temperature due to the size reduction of the clusters by re-evaporation that consequently would create defects. Similarly, the application of short time (30 min) leads to high defects ($I(D)/I(G) = 2.4$) because the radical

formations and nucleation sites are not formed enough. Here, the influence of the Ar flux is weak.

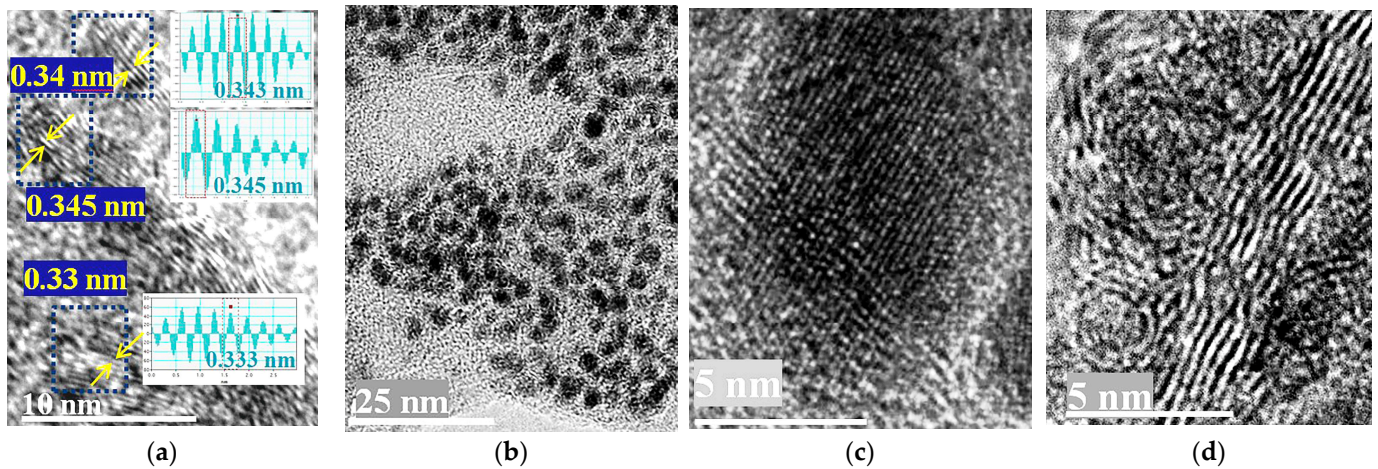


Figure 3. TEM images. (a) Interlayer spaces of the walls. (b,c) Graphene nanocrystallites inside the CNWs sample with a diameter around 9 nm. (b) In-plane lattice fringes. (d) Nanoparticles with curved layers inside the CNWs sample.

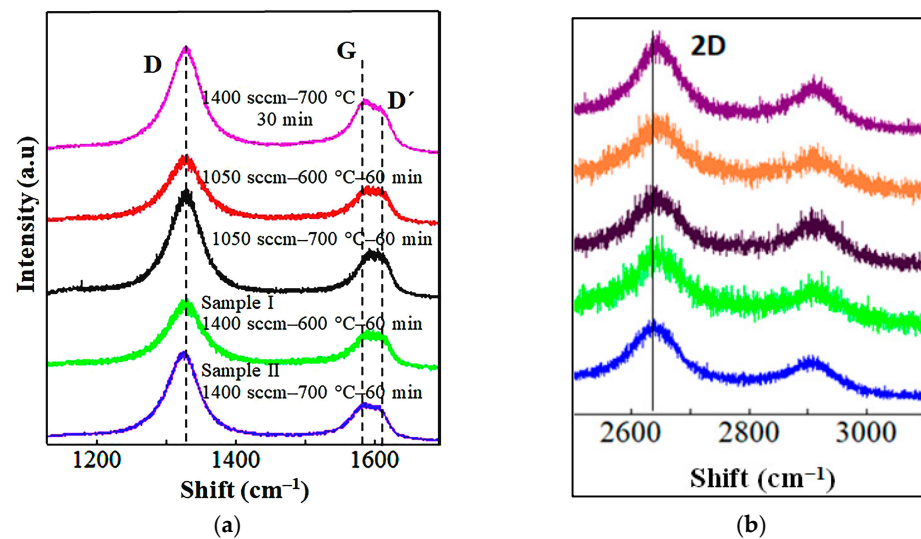


Figure 4. The RAMAN spectra for the CNWs grown at 30 min with 1400 sccm-700 °C (purple line) and at 60 min with 1050 sccm-600 °C (red line), 1050 sccm-700 °C (black line), 1400 sccm-600 °C (green line) and 1400 sccm-700 °C (blue line). The figure includes (a) the D and G bands and (b) 2D bands.

Different types of defects can be defined, such as edges, grain boundaries, vacancies, substitutional and implanted atoms, and a change of carbon hybridization (for example, from sp^2 into sp^3) [33]. The average defect distance between the point defects (L_D) can be related to the invers $I(D)/I(G)$, using the following equation [34]:

$$L_D^2(\text{nm}^2) = \frac{C_D}{E_L^4} \frac{I(G)}{I(D)} \quad (2)$$

where $C_d = 3600$ and E_L is the excitation laser energy used in the Raman experiment (1.96 eV). Table 1 reveals the values obtained. The nature of the defects can be identified by the $I(D)/I(D')$ relation. According to Eckmann et al. [35], the $I(D)/I(D')$ around 3.5 is attributed to boundary-like defects in graphite-related materials. As a consequence, the values presented in Table 1 show that the disorder-induced bands would occurs principally

from aggregates of crystallite border (one-dimensional defects) [36], which are the most common case of disorder [37]. The crystallite sizes (L_a) can be related to the inverts $I(D)/I(G)$, using the following equation [38]:

$$L_a(\text{nm}) = \frac{C_a I(G)}{E_L^4 I(D)} \quad (3)$$

where $C_a = 560$. Therefore, the increase of the $I(D)/I(G)$ with temperature causes the disassembly of the graphene layers into nanocrystals (Sample I, $L_a = 21.1$ nm and Sample II, $L_a = 17.3$ nm) with an increase of their population. These values are approximated since many papers have modified the respective equations. For example, Mallet et al. [39] regarded $C_a = 4.4 \times (2.41)^4$ and Ribeiro-Soares et al. [40] $C_a = (490 \pm 100) \times 10^3$. In this sense, the L_a calculated here approximates to the GNs size observed in TEM images (~9 nm).

Interesting, the 2D band (see Figure 4b) shows a single Lorentzian deconvolution—which is a hallmark of few layers [41], but with a low intensity comparable to graphite [42]. The shift of this band to low frequencies corresponds to a reduction of the graphene-layer numbers [43]. Increasing both the temperature and the Ar flux, the lower value of the 2D position (see Figure 4b and Table 1) appears on Sample II at 2639 cm^{-1} (blue line). Thus, it behaves more like graphene structure with a few layers [43].

The X-ray photoelectron spectra (Figure 5a,b) and the ERDA measurements (Figure 5c) reveal the relative atomic concentrations of the carbon and oxygen atoms, and the hydrogen content in the CNWs, respectively. The oxygen is binding from moderate vacuum, substrate or atmospheric ambient, which creates more irreversible doping. The relative concentration of oxygen (percent) is reduced as the Ar flux increases or temperature decreases, in association with the defect decline. In addition, this occurs at the expense of the increment of the carbon atoms. Thus, the graphitization is observed on Samples I (green line) and Sample II (blue line). The high carbon concentration around 86.44% on Sample I (see Table 1) is confirmed with the position of the C1s band at 284.3 eV related to the $\text{Sp}^2 \text{C}=\text{C}$ binding (see the green line in Figure 5b). Additionally, the ERDA measurements show that the Sample I and Sample II do not incorporate large amounts of hydrogen either. The nanostructure growth for 30 min (purple line) presents a lower amount of hydrogen because of the incipient formation of the graphene layers; however, a posterior study should be performed to evaluate the oxygen content.

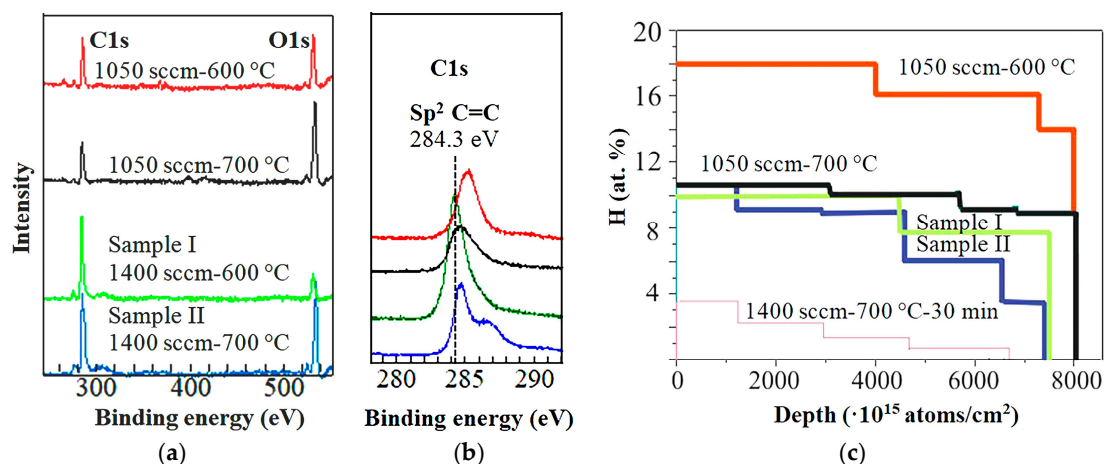


Figure 5. (a,b) The XPS spectra and (c) the ERDA measurements for the CNWs grown at 1050 sccm-600 °C-60 min (red line), 1050 sccm-700 °C-60 min (black line), 1400 sccm-600 °C-60 min (green line) and 1400 sccm-700 °C-60 min (blue line). The figure includes in (a) the C1s and O1s bands, (b) the amplification of the C1s band and (c) the hydrogen content along the transversal section (depth) of the samples, including 1400 sccm-700 °C-30 min (purple line).

3.2. Magnetoresistance

The Sample I and Sample II were selected for the magnetotransport studies because they present different grades of disorder and, at the same time, have attractive structural and morphological qualities, such as few graphene layers in the walls, large dimensions, high graphitization and a reduced contamination by hydrogen or oxygen atoms. The oxygen bonded in the graphene lattice or on the basal plane produces a charge transfer [44] and the carrier concentration of the CNWs becomes slightly higher [45].

3.2.1. Sample I, Low Disorder

The interference effect between the charges' carriers is most pronounced in low-dimensional systems (such as graphene) because there are higher probabilities to intersect their own path, leading to the weak localization (WL). The McCann's model [46] is used to confirm the presence of weak localization and antilocalization. It points out that the phase of interference correction to the magnetoresistance in graphene can be expressed as follows:

$$\Delta R = -R^2 \frac{e^2}{\pi h} \left[F\left(\frac{2\tau_\phi}{\tau_B}\right) - F\left(\frac{2}{\tau_B(\tau_\phi^{-1} + 2\tau_i^{-1})}\right) - 2F\left(\frac{2}{\tau_B(\tau_\phi^{-1} + \tau_i^{-1} + \tau_s^{-1})}\right) \right] \quad (4)$$

where $\Delta R = R(B) - R(0)$, $F(z) = \ln Z + \psi\left(\frac{1}{2} + \frac{1}{z}\right)$ and ψ is the Digamma Function. Moreover, $\tau_B = \frac{h}{2eDB}$, $\tau_s^{-1} = \tau_s^{-1} + \tau_w^{-1}$, D is the diffusion coefficient and e de charge of electron. The τ_w^{-1} and τ_s^{-1} are the trigonal warping and elastic scattering rate, respectively. The intervalley scattering τ_i^{-1} is an elastic process wherein a charge is scattered from the edges or defects with the size of the order of the lattice space (adatoms and vacancies) [47], while the phase coherence τ_ϕ^{-1} is originated via electron-phonon scattering. The quantum correction to the conductivity occurs when $\tau_\phi^{-1} < \tau_i^{-1}$. The first term in Equation (4) corresponds to WL, while both the second and third terms correspond to WAL.

Figure 6a shows the ΔR as a function of the magnetic field for Sample I. The good fit with the McCann's model (represented in black lines) confirms the apparition of the WL and WAL effect. The transition from WL to WAL occurs around 0.7 T, at low temperature (below 100 K), with a displacement along the x-axis for higher temperatures (above 100 K). This last one corresponds to the reduction of the $\tau_\phi^{-1}/\tau_i^{-1}$ relation (3.5 to 2.7 for T = 100 K and T = 250 K, respectively); see Figure 6b, the green line. Above 100 K, the τ_i^{-1} increases with more rate than τ_ϕ^{-1} , probably by an addition of electron-like carriers from interfaces and impurities (interstitials, excess atoms or ions). In Figure 6b (red line), the temperature causes an increment of the number of phonons, which could be released from the substrate, thus improving the phase coherence τ_ϕ^{-1} .

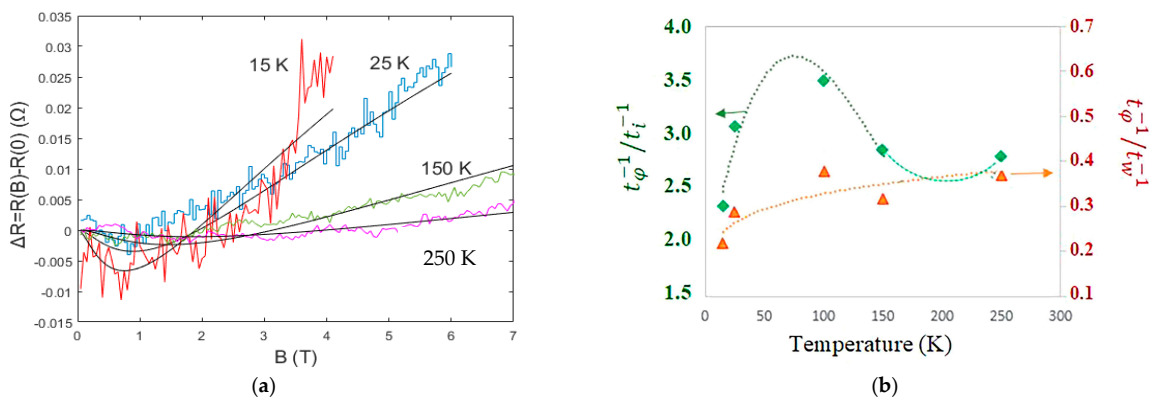
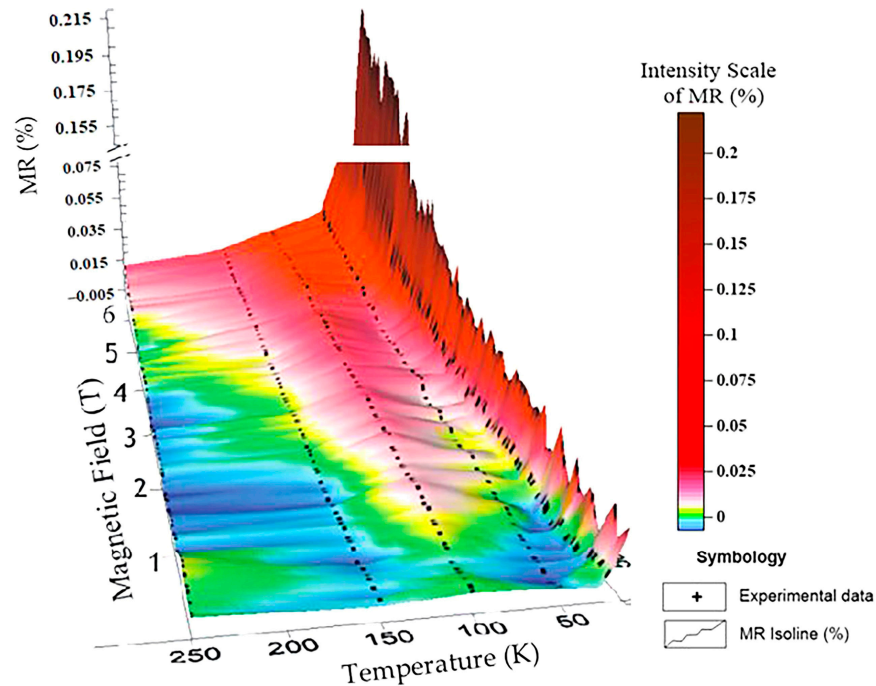
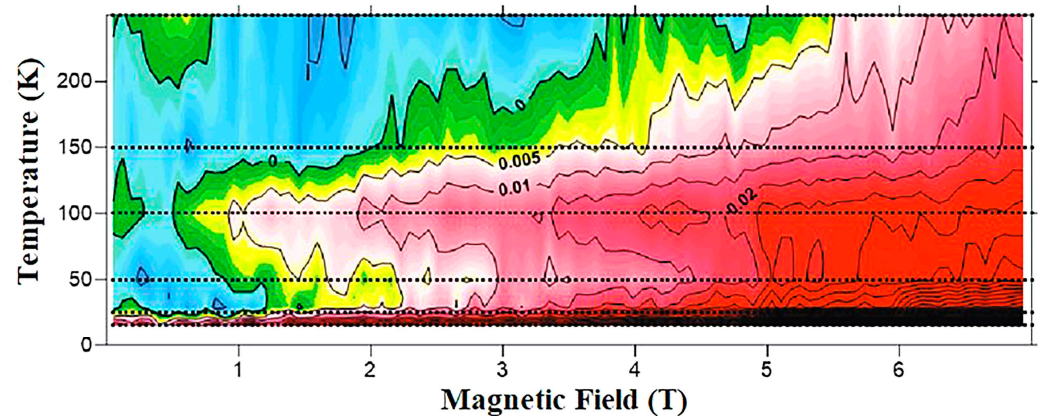


Figure 6. (a) The best fit on Sample I by the model of McCann (black line) with the experimental curves of $\Delta R = R(B) - R(0)$ as a function of the magnetic field at different temperatures. (b) The $\tau_\phi^{-1}/\tau_i^{-1}$ and $\tau_\phi^{-1}/\tau_w^{-1}$ rates obtained through the best fit with the τ_w^{-1} fixed.

A general view of the WL-to-WAL transition can be seen in Figure 7a, which represents the 3D magnetoresistance as a function of the magnetic field and temperature. It denotes an evident crossover around 100 K, where, above this temperature, the negative values of MR (blue region) achieve a higher magnetic field.



(a)



(b)

Figure 7. (a) Three-dimensional image of the MR in function of the temperature and the magnetic field of Sample I. (b) Isoline map of the MR.

3.2.2. Sample II, High Disorder

Sample II shows a linear positive MR only below 2 T on approximately all ranges of temperature (40–75 K and 120–250 K) and a negative MR for the higher magnetic field (see Figures 8 and 9a). The MR varies fundamentally with the magnetic field and slightly with the temperature.

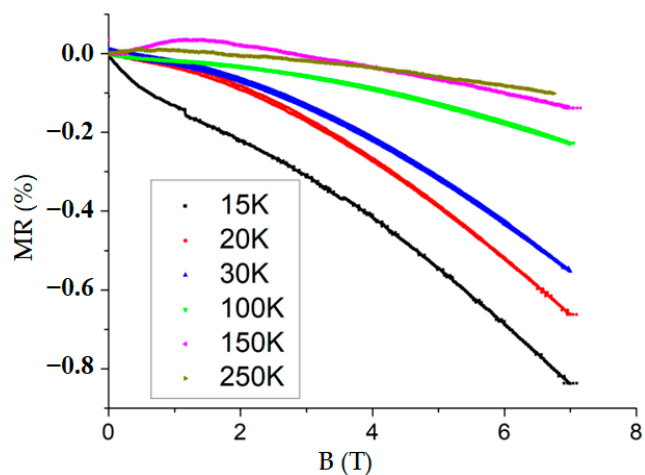


Figure 8. The MR measurement of Sample II.

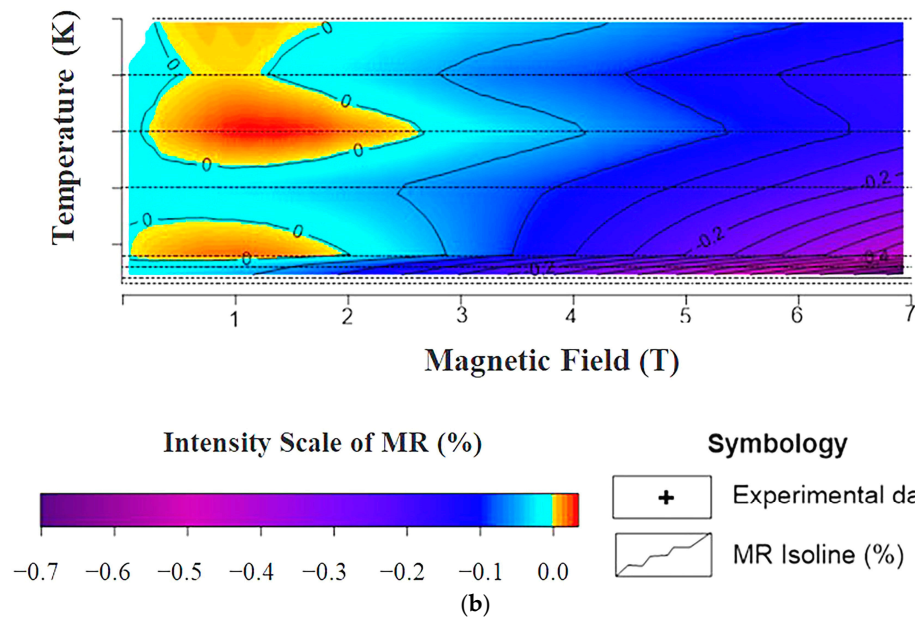
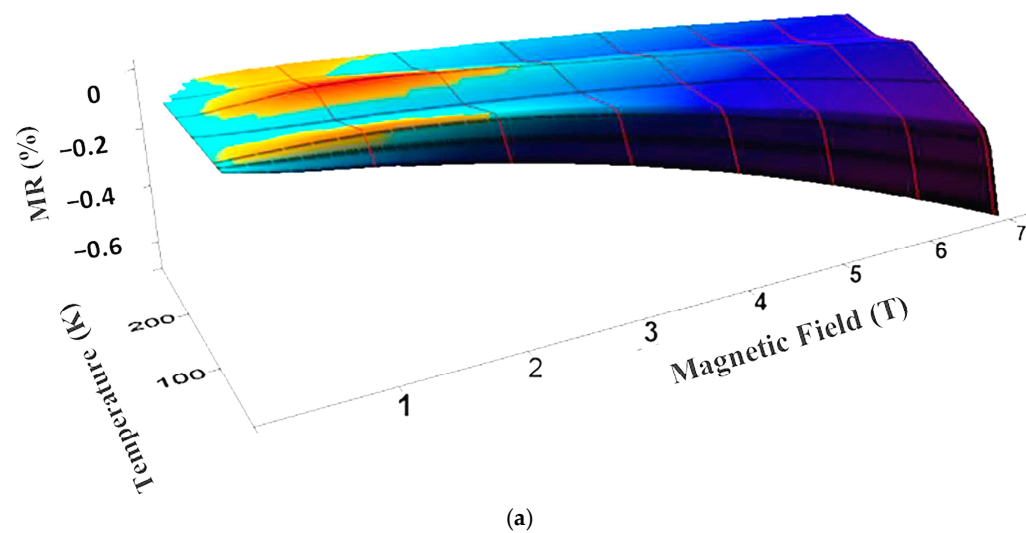


Figure 9. (a) Three-dimensional image of the MR in function of the temperature and the magnetic field of Sample II. (b) Isoline map of the MR.

The transition from WL to WAL is suppressed for Sample II. The linear positive MR at low field (below 2 T) could be associated with in-plane graphene transport via a hopping mechanism due to the large number of defects. This is in agreement with the results obtained by Kovelevich and coworkers [48] in graphite with disorder and Shlimak and collaborators [49] in irradiated monolayer. The process is based on the spin polarization and the electron–electron interaction [50]. At a low magnetic field, the spin polarization of localized electrons into a single graphene layer dominates rather than magneto-orbital effects. As the magnetic field increases, more localized sites present a spin aligned to the field, and the hops are suppressed through Pauli blockade, leading to a positive MR [51]. This positive MR has no limitation for the observation at high temperatures, which is consistent with our result. Above 2 T, the hops are canceled due to the Pauli blockade, and the transport is dominated by diffusion of electrons associated with the negative and quadratic magnetic field dependence of the MR. The electronic charges could be scattered among graphene nanocrystallites that reduce the carrier mean free path. Zhou and collaborators [52] also reported the effect on the graphene monolayer. The negative diffusion magnetoresistance, MR_{Ds} , is given by the following:

$$MR_{Ds} = -\frac{\Delta l}{l_0} = -KB^2 \quad (5)$$

where Δl is the increment of the mean free path of the charge carriers caused by the magnetic field, l_0 is the mean free path of the carrier without magnetic field and K is a constant [5]. The lengthening of the mean free path with greater magnetic field leads to a negative MR_{Ds} .

3.2.3. MR Isoline Maps

The MR isoline maps for both samples (Figures 7b and 9b) show below 50 K an increase of the isoline density related to an increase of the MR variation. This effect is characteristic of the network structure and independent of the number of defects. For making a clear interpretation, we carried out measurements of the magnetic moment depending on the temperature, $m(T)$ (see Figure 10). A maximum value of the magnetization curve is observed around 65 K, indicating the presence of magnetic entities. Davami and collaborators [21] also reported such behavior at $T = 50$ K as a result of magnetic phase transitions. Fernandez-Rossier and collaborators [53] reported a coexistence between antiferromagnetic and ferromagnetic order for graphene. Different origins may cause the magnetic entities, such as the presence of carbon nanoparticles [54], the ion bombardment [55] over the sample during the deposition, defects such as domains and interfaces, and chemisorption of hydrogen and oxygen [56,57].

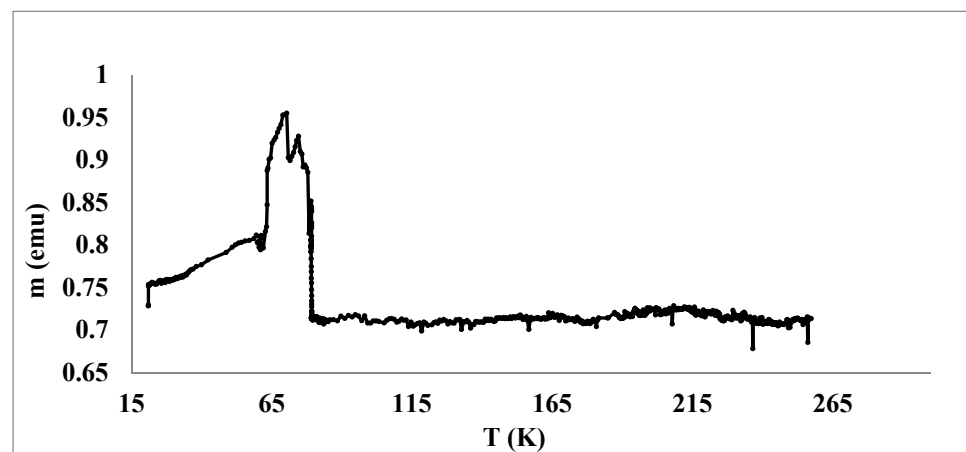


Figure 10. Magnetic moment as a function of the temperature of Sample I.

The maximum of the magnetization occurs approximately in the time with the variation the MR isoline density at 50 K. During the sweeping of the magnetic field to 7 T in the MT measurements, the electrons are spin-polarized with the field, and the scattering effect would be spin dependent, which should cause the variation of the MR isoline density.

4. Conclusions

The variation of the deposition temperature strongly modified the disorder and graphitization of the CNWs, and this, in turn, modified the magnetotransport properties. Sample I revealed a negative MR caused by weak localization in the presence of defects and a transition to the WAL effect, as is characteristic to the in-plane graphene transport. However, the highly disordered structure, Sample II, led to the Hopping mechanism and a diffusion transport from extrinsic electron scattering on graphene nanocrystallites. At a low temperature (15 K), Sample I enhanced a maxim $|MR|$ at 0.2%, while Sample II at 0.8%. The MR isoline maps for both samples show, below 50 K, an increase of the isoline density associated with the presence of magnetic entities. The microstructural tunability of the CNWs obtained introduces new perspectives for magneto-electronic devices.

Author Contributions: Formal analysis, investigation, software, writing—original draft, review and editing preparation, M.A.G.; methodology, S.V., M.V., R.G.G. and S.A.; conceptualization, R.G.G., M.A.G. and R.A.R.-C.; Validation, S.V., M.V., S.A., J.J.A.P., R.A.R.-C. and G.D.; Resources, project administration, funding acquisition, R.A.R.-C., J.M.P., J.J.A.P., M.V., G.D. and M.A.G.; Data curation, M.A.G., S.V., S.A. and J.J.A.P. All authors have read and agreed to the published version of the manuscript.

Funding: This work was financial supported for J.M.P. through CONACYT Programme, Mexico; M.A.G. and J.J.A.P. by the postdoctoral programme from the Meritorious Autonomous University of Puebla (BUAP), Mexico; G.D. from the National Institute for Lasers, Plasma and Radiation Physics (INFLPR), Romania, and R.A.R.-C. from University of Guanajuato, Mexico. M.V. acknowledges the financial support of a grant of the Ministry of Research, Innovation and Digitization, CCCDI—UEFISCDI, project number PN-III-P2-2.1-PED-2021-3112, 597PED/2022, within PNCDI III.

Institutional Review Board Statement: Not applicable.

Informed Consent Statement: Not applicable.

Data Availability Statement: Not applicable.

Acknowledgments: We want to thank Ion Burducea for ERDA research and Roberto Mora Monroy for XPS measurements.

Conflicts of Interest: The authors declare no conflict of interest. The funders had no role in the design of the study; in the collection, analyses, or interpretation of data; in the writing of the manuscript; or in the decision to publish the results.

References

1. Tikhonenko, F.V.; Horsell, D.W.; Gorbachev, R.V.; Savchenko, A.K. Weak localization in graphene flakes. *Phys. Rev. Lett.* **2008**, *100*, 056802–056805. [[CrossRef](#)]
2. Liu, Y.; Lew, W.S.; Sun, L. Enhanced weak localization effect in few-layer graphene. *Phys. Chem. Chem. Phys.* **2011**, *13*, 20208–20214. [[CrossRef](#)] [[PubMed](#)]
3. Kechedzhi, K.; Fal'ko, V.I.; McCann, E.; Altshuler, B.L. Influence of trigonal warping on interference effects in bilayer graphene. *Phys. Rev. Lett.* **2007**, *98*, 176806–176809. [[CrossRef](#)]
4. Ki, D.K.; Jeong, D.; Choi, J.H.; Lee, H.J. Inelastic scattering in a monolayer graphene sheet; a weak-localization study. *Phys. Rev. B* **2008**, *78*, 125409–125413. [[CrossRef](#)]
5. Zhang, X.; Xue, Q.; Zhu, D. Positive and negative linear magnetoresistance of graphite. *Phys. Lett. A* **2004**, *320*, 471–477. [[CrossRef](#)]
6. Morpurgo, A.F.; Guinea, F. Intervalley scattering, long-range disorder, and effective time-reversal symmetry breaking in graphene. *Phys. Rev. Lett.* **2006**, *97*, 196804–196807. [[CrossRef](#)] [[PubMed](#)]
7. Lara-Avila, S.; Tzalenchuk, A.; Kubatkin, S.; Yakimova, R.; Janssen, T.; Cedergren, K.; Bergsten, T.; Falko, V. Disordered Fermi Liquid in Epitaxial Graphene from Quantum Transport Measurements. *Phys. Rev. Lett.* **2011**, *107*, 166602–166606. [[CrossRef](#)] [[PubMed](#)]

8. Esquinazi, P.; Krüger, J.; Barzola-Quiquia, J.; Schönemann, R.; Herrmannsdörfer, T.; García, N. On the low-field Hall coefficient of graphite. *AIP Adv.* **2014**, *4*, 117121. [[CrossRef](#)]
9. Li, J.; Liu, Z.; Guo, Q.; Yang, S.; Xu, A.; Wang, Z.; Wang, G.; Wang, Y.; Chen, D.; Ding, G. Controllable growth of vertically oriented graphene for high sensitivity gas detection. *J. Mater. Chem. C* **2019**, *7*, 5995–6003. [[CrossRef](#)]
10. Zhai, Z.; Leng, B.; Yang, N.; Yang, B.; Liu, L.; Huang, N.; Jiang, X. Rational Construction of 3D-Networked Carbon Nanowalls/Diamond Supporting CuO Architecture for High-Performance Electrochemical Biosensors. *Small* **2019**, *15*, 1901527. [[CrossRef](#)] [[PubMed](#)]
11. Dinh, T.; Achour, A.; Vizireanu, S.; Dinescu, G.; Nistor, L.; Armstrong, A.; Guay, D.; Pech, D. Hydrous RuO₂/carbon nanowalls hierarchical structures for all-solid-state ultrahigh-energy-density micro-supercapacitors. *Nano Energy* **2014**, *10*, 288–294. [[CrossRef](#)]
12. Hung, T.-C.; Chen, C.-F.; Whang, W.-T. Deposition of carbon nanowall flowers on two-dimensional sheet for electrochemical capacitor application. *Electrochem. Solid-State Lett.* **2009**, *12*, 6. [[CrossRef](#)]
13. Yue, Z.; Levchenko, I.; Kumar, S.; Seo, D.; Wang, X.; Doua, S.; Ostrikov, K. Large networks of vertical multi-layer graphenes with morphology-tunable magnetoresistance. *Nanoscale* **2013**, *5*, 9283–9288. [[CrossRef](#)]
14. Huang, J.; Guo, L.-W.; Li, Z.-L.; Chen, L.-L.; Lin, J.-J.; Jia, Y.-P.; Lu, W.; Guo, Y.; Chen, X.-L. Anisotropic quantum transport in a network of vertically aligned graphene sheets. *J. Phys. Condens. Matter* **2014**, *26*, 345301. [[CrossRef](#)]
15. Hiramatsu, M.; Nihashi, Y.; Kondo, H.; Hori, M. Nucleation Control of Carbon Nanowalls Using Inductively Coupled Plasma-Enhanced Chemical Vapor Deposition. *Jpn. J. Appl. Phys.* **2013**, *52*, 01AK05. [[CrossRef](#)]
16. Lin, J.; Guo, L.; Huang, Q.; Jia, Y.; Li, K.; Lai, X.; Chen, X. Anharmonic phonon effects in Raman spectra of unsupported vertical graphene sheets. *Phys. Rev. B* **2011**, *83*, 125430. [[CrossRef](#)]
17. Zhang, H.; Kikuchi, N.; Kogure, T.; Kusano, E. Growth of carbon with vertically aligned nanoscale flake structure in capacitively coupled rf glow discharge. *Vacuum* **2008**, *82*, 754–759. [[CrossRef](#)]
18. Shang, N.G.; Au, F.C.K.; Meng, X.M.; Lee, C.S.; Bello, I.; Lee, S.T. Uniform carbon nanoflake films and their field emissions. *Chem. Phys. Lett.* **2002**, *358*, 187–191. [[CrossRef](#)]
19. Tanaka, K.; Yoshimura, M.; Okamoto, A.; Ueda, K. Growth of carbon nanowalls on a SiO₂ substrate by microwave plasma-enhanced chemical vapor deposition. *Jpn. J. Appl. Phys.* **2005**, *44*, 2074–2076. [[CrossRef](#)]
20. Vesel, A.; Zaplotnik, R.; Primc, G.; Mozetič, M. Synthesis of Vertically Oriented Graphene Sheets or Carbon Nanowalls—Review and Challenges. *Materials* **2019**, *12*, 2968. [[CrossRef](#)]
21. Davami, K.; Shaygan, M.; Kheirabi, N.; Zhao, J.; Kovalenko, D.A.; Rummeli, M.H.; Opitz, J.; Cuniberti, G.; Lee, J.-S.; Meyyappan, M. Synthesis and characterization of carbon nanowalls on different substrates by radio frequency plasma enhanced chemical vapor deposition. *Carbon* **2014**, *72*, 372. [[CrossRef](#)]
22. Vizireanu, S.; Mitu, B.; Luculescu, C.; Nistor, L.; Dinescu, G. PECVD synthesis of 2D nanostructured carbon material. *Surf. Coat. Technol.* **2012**, *211*, 2–8. [[CrossRef](#)]
23. Zhang, H.; Wu, S.; Lu, Z.; Chen, X.; Chen, Q.; Gao, P.; Yu, T.; Peng, Z.; Ye, J. Efficient and controllable growth of vertically oriented graphene nanosheets by mesoplasma chemical vapor deposition. *Carbon* **2019**, *147*, 341–347. [[CrossRef](#)]
24. Lenz, J.E. A review of magnetic sensors. *Proc. IEEE* **1990**, *78*, 973. [[CrossRef](#)]
25. Daughton, J.M. GMR applications. *J. Magn. Magn. Mater.* **1999**, *192*, 334. [[CrossRef](#)]
26. Acosta Gentoiu, M.; Betancourt-Riera, R.; Vizireanu, S.; Burducea, I.; Marascu, V.; Stoica, S.D.; Bitu, B.I.; Dinescu, G.; Riera, R. Morphology, Microstructure and Hydrogen content of Carbon Nanostructures Obtained by PECVD at Various Temperatures. *J. Nanomater.* **2017**, *2017*, 1374973. [[CrossRef](#)]
27. Vizireanu, S.; Ionita, M.D.; Ionita, R.E.; Stoica, S.D.; Teodorescu, C.M.; Husanu, M.A.; Apostol, N.G.; Baibarac, M.; Panaitescu, D.; Dinescu, G. Aging phenomena and wettability control of plasma deposited carbon nanowall layers. *Plasma Process. Polym.* **2017**, *14*, 1700023. [[CrossRef](#)]
28. Vizireanu, S.; Ionita, M.D.; Dinescu, G.; Enculescu, I.; Baibarac, M.; Baltog, I. Post-synthesis carbon nanowalls transformation under hydrogen, oxygen, nitrogen, tetrafluoroethane and sulfur hexafluoride plasma treatments. *Plasma Process. Polym.* **2012**, *9*, 363–370. [[CrossRef](#)]
29. Kobayashi, K.; Tanimura, M.; Nakai, H.; Yoshimura, A.; Yoshimura, H.; Kojima, K.; Tachibana, M. Nanographite domains in carbon nanowalls. *J. Appl. Phys.* **2007**, *101*, 94306. [[CrossRef](#)]
30. Baskin, Y.; Meyer, L. Lattice Constants of Graphite at Low Temperatures. *Phys. Rev.* **1955**, *100*, 544. [[CrossRef](#)]
31. Gomez-Hernandez, R.; Panecatl-Bernal, Y.; Mendez-Rojas, M.A. High yield and simple one-step production of carbon black nanoparticles from waste tires. *Heliyon* **2019**, *5*, e02139. [[CrossRef](#)]
32. Tuinstra, F.; Koenig, J.L. Raman Spectrum of Graphite. *J. Chem. Phys.* **1970**, *53*, 1126. [[CrossRef](#)]
33. Eckmann, A.; Felten, A.; Verzhbitskiy, I.; Davey, R.; Casiraghi, C. Raman study on defective graphene: Effect of the excitation energy, type, and amount of defects. *Phys. Rev. B* **2013**, *88*, 035426–035436. [[CrossRef](#)]
34. Sozaraj, S.R.; Caridad, J.M.; Schulte, L.; Cagliani, A.; Borah, D.; Morris, M.A.; Bøggild, P.; Ndoni, S. High quality sub-10 nm graphene nanoribbons by on-chip PS-b-PDMS block copolymer lithography. *RSC Adv.* **2015**, *5*, 66711.
35. Eckmann, A.; Felten, A.; Mishchenko, A.; Britnell, L.; Krupke, R.; Novoselov, K.S.; Casiraghi, C. Probing the Nature of Defects in Graphene by Raman Spectroscopy. *Nano Lett.* **2012**, *12*, 925–930. [[CrossRef](#)]

36. Cañado, L.G.; Jorio, A.; Ferreira, E.H.M.; Stavale, F.; Achete, C.; Capaz, R.B.; Moutinho, M.V.O.; Lombardo, A.; Kulmala, T.S.; Ferrari, A.C. Quantifying Defects in Graphene via Raman Spectroscopy at Different Excitation Energies. *Nano Lett.* **2011**, *11*, 3190–3196. [[CrossRef](#)]
37. Pimenta, M.A.; Dresselhaus, G.; Dresselhaus, M.S.; Cancado, L.G.; Jorio, A.; Saito, R. Studying disorder in graphite-based systems by Raman spectroscopy. *Phys. Chem. Chem. Phys.* **2007**, *9*, 1276–1291. [[CrossRef](#)]
38. Cañado, L.G.; Takai, K.; Enoki, T.; Endo, M.; Kim, Y.A.; Mizusaki, H.; Jorio, A.; Coelho, L.N.; Magalhães-Paniago, R.; Pimenta, M.A. General equation for the determination of the crystallite size L_a of nanographite by Raman spectroscopy. *Appl. Phys. Lett.* **2006**, *88*, 163106. [[CrossRef](#)]
39. Mallet-Ladeira, P.; Puech, P.; Toulouse, C.; Cazayous, M.; Ratel-Ramond, N.; Weisbecker, P.; Vignoles, G.L.; Monthieux, M. A Raman study to obtain crystallite size of carbon materials: A better alternative to the Tuinstra–Koenig law. *Carbon* **2014**, *80*, 629–639. [[CrossRef](#)]
40. Ribeiro-Soares, J.; Olivero, M.E.; Garinc, C.; David, M.V.; Martins, L.G.P.; Almeida, C.A.; Martins-Ferreira, E.H.; Takai, K.; Enoki, T.; Magalhães-Paniago, R.; et al. Structural analysis of polycrystalline graphene systems by Raman spectroscopy. *Carbon* **2015**, *95*, 646–652. [[CrossRef](#)]
41. Reina, A.; Jia, X.; Ho, J.; Nezich, D.; Son, H.; Bulovic, V.; Dresselhaus, M.S.; Kong, J. Large area, few-layer graphene films on arbitrary substrates by chemical vapor deposition. *Nano Lett.* **2008**, *9*, 30–35. [[CrossRef](#)]
42. Ferrari, A.C.; Meyer, J.C.; Scardaci, V.; Casiraghi, C.; Lazzeri, M.; Mauri, F.; Piscanec, S.; Jiang, D.; Novoselov, S.; Roth, S.; et al. Raman Spectrum of Graphene and Graphene Layers. *Phys. Rev. Lett.* **2006**, *97*, 187401. [[CrossRef](#)] [[PubMed](#)]
43. Ni, Z.; Wang, Y.; Yu, T.; Shen, Z. Raman spectroscopy and imaging of graphene. *Nano Res.* **2008**, *1*, 273–291. [[CrossRef](#)]
44. Mackenzie, D.; Galbiati, M.; Cerio, X.; Sahalianov, I.; Radchenko, T.; Sun, J.; Peña, D.; Gammelgaard, L.; Jessen, B.; Thomsen, J.; et al. Unraveling the electronic properties of graphene with substitutional oxygen. *2D Mater.* **2021**, *8*, 045035. [[CrossRef](#)]
45. Takeuchi, W.; Takeda, K.; Hiramatsu, M.; Tokuda, Y.; Kano, H.; Kimura, S.; Sakata, O.; Tajiri, H.; Hori, M. Monolithic self-sustaining nanographene sheet grown using plasma-enhanced chemical vapor deposition. *Phys. Status Solidi (A)* **2010**, *207*, 139–143. [[CrossRef](#)]
46. McCann, E.; Kechedzhi, K.; Fal'ko, V.I.; Suzuura, H.; Ando, T.; Altshuler, B.L. Weak localization magnetoresistance and valley symmetry in graphene. *Phys. Rev. Lett.* **2006**, *97*, 146805–146808. [[CrossRef](#)] [[PubMed](#)]
47. Pezzini, S.; Cobaleda, C.; Diez, E.; Bellani, V. Disorder and de-coherence in graphene probed by low-temperature magnetotransport: weak localization and weak antilocalization. *J. Phys. Conf. Ser.* **2013**, *456*, 012032. [[CrossRef](#)]
48. Kopelevich, Y.; da Silva, R.R.; Camargo, B.C.; Alexandrov, A.S. Extraordinary magnetoresistance in graphite: Experimental evidence for the time-reversal symmetry breaking. *J. Phys. Condens. Matter* **2013**, *25*, 466004. [[CrossRef](#)] [[PubMed](#)]
49. Shlimak, I.; Zion, E.; Butenko, A.; Wolfson, L.; Richter, V.; Kaganovskii, Y.; Sharoni, A.; Haran, A.; Naveh, D.; Kogan, E.; et al. Hopping magnetoresistance in ion irradiated monolayer graphene. *Phys. E Low-Dimens. Syst. Nanostruct.* **2016**, *76*, 158–163. [[CrossRef](#)]
50. Kamimura, H.; Kurobe, A.; Takemori, T. Magnetoresistance in Anderson-localized systems. *Physica B+C* **1983**, *117–118*, 652. [[CrossRef](#)]
51. Zhao, H.L.; Spivak, B.Z.; Gelfand, M.P.; Feng, S. Negative magnetoresistance in variable-range-hopping conduction. *Phys. Rev. B* **1991**, *44*, 10760–10767. [[CrossRef](#)] [[PubMed](#)]
52. Zhou, Y.B.; Han, B.H.; Liao, Z.M.; Wu, H.C.; Yu, D.P. From positive to negative magnetoresistance in graphene with increasing disorder. *Appl. Phys. Lett.* **2011**, *98*, 222502. [[CrossRef](#)]
53. Fernandez-Rossier, J.; Palacios, J.J. Magnetism in graphene nanoislands. *Phys. Rev. Lett.* **2007**, *99*, 177204. [[CrossRef](#)] [[PubMed](#)]
54. Parkanskya, N.; Alterkopa, B.; Boxmana, R.L.; Leitusb, G.; Berkhc, O.; Barkayd, Z.; Rosenberg, Y.; Eliaz, N. Magnetic properties of carbon nano-particles produced by a pulsed arc submerged in ethanol. *Carbon* **2008**, *46*, 215–219. [[CrossRef](#)]
55. Esquinazi, P.; Spemann, D.; Höhne, R.; Setzer, A.; Han, K.-H.; Butz, T. Induced magnetic ordering by proton irradiation in graphite. *Phys. Rev. Lett.* **2003**, *91*, 227201. [[CrossRef](#)] [[PubMed](#)]
56. Kusakabe, K.; Maruyama, M. Magnetic nanographite. *Phys. Rev. B* **2003**, *67*, 092406. [[CrossRef](#)]
57. Yazyev, O.V. Magnetism in disordered graphene and irradiated graphite. *Phys. Rev. Lett.* **2008**, *101*, 037203. [[CrossRef](#)] [[PubMed](#)]

Disclaimer/Publisher's Note: The statements, opinions and data contained in all publications are solely those of the individual author(s) and contributor(s) and not of MDPI and/or the editor(s). MDPI and/or the editor(s) disclaim responsibility for any injury to people or property resulting from any ideas, methods, instructions or products referred to in the content.